

Exploring the feasibility of SS316L fabrication via CMT-based WAAM: A Comprehensive study on microstructural, mechanical and tribological properties

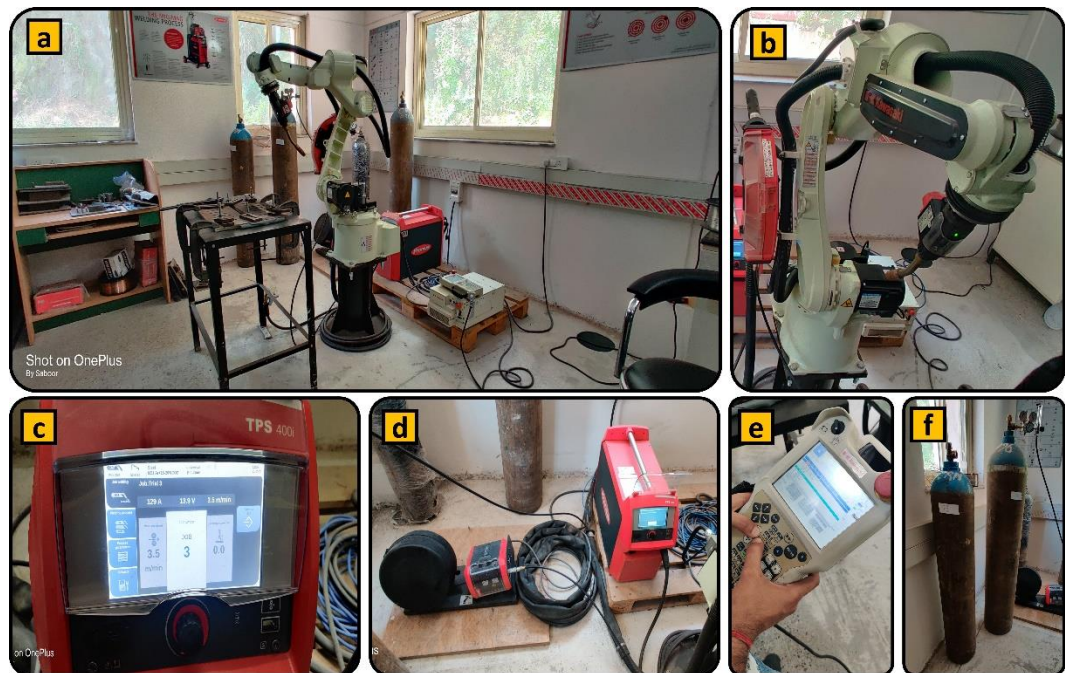
Saboor Fayaz Lone¹, Dinesh Wasudeo Rathod^{2*}, Sheikh Nazir Ahmad¹

¹ Department of Mechanical Engineering, NIT Srinagar J&K, Jammu and Kashmir 190006, India

² Department of Mechanical Engineering, NIT Kurukshetra, Haryana 136119, India

✉ dineshvrathod@gmail.com, dinesh.rathod@nitkr.ac.in

This article
contributes to:



Highlights:

- CMT-based WAAM: Deposited multi-layered SS316L with seamless fusion and no defects.
- Material Properties: Grain size increased, reducing hardness, strength, but maintaining ductility.
- Tribological Performance: Higher wear rate and friction, with abrasive wear mechanisms confirming durability.

Article info

Submitted:

2024-07-20

Revised:

2024-11-07

Accepted:

2024-11-07



This work is licensed under
a Creative Commons
Attribution-NonCommercial 4.0
International License

Publisher

Universitas Muhammadiyah
Magelang

Abstract

Additive manufacturing (AM) is revolutionizing production, enabling the customization of components for specific applications while promoting sustainable and on-demand manufacturing. This innovative method is especially valuable for producing intricate and custom parts from metallic materials like SS316L. Known for its excellent corrosion resistance and high strength, AISI 316L austenitic steel is widely utilized in aerospace, medical, automotive, and marine industries. This study explores the deposition of multi layered SS316L wall using the Cold Metal Transfer (CMT)-based Wire Arc Additive Manufacturing (WAAM) technique. The resultant multilayered wall exhibited seamless fusion devoid of macroscopic defects. A comprehensive analysis of its morphology, microstructure, mechanical properties, and tribological performance was conducted. Microstructural examination revealed a progression from fine equiaxed grains with ferrites in the lower sections to coarser columnar grains with acicular ferrites in the upper sections. Vickers microhardness and Charpy impact tests indicated a decline in hardness and impact energy from lower to upper sections. Uniaxial tensile tests demonstrated decreasing yield and ultimate tensile strengths, alongside significant ductility and toughness. The coefficient of friction and wear rate escalated with higher loads and from lower to upper sections, predominantly displaying abrasive

wear mechanisms. These results validate the efficacy and durability of the SS316L CMT-based WAAM process in fabricating high-quality structures with tailored mechanical and tribological properties.

Keywords: Tribological Properties; Wear; Low Heat; Equiaxed Grains

1. Introduction

Conventional methods for manufacturing machine parts predominantly involve casting and forging processes [1]. Nonetheless, the creation of molds essential for these procedures entails significant machining expenses and extensive time, rendering this mode of production unsuitable for the escalating need for custom-made part modifications and the rapidly evolving nature of product updates. Moreover, this age-old technique proves ineffective for components with highly intricate internal structures or those necessitating seamless integration during formation [2]. Additive manufacturing (AM) is a cutting-edge technology that fabricates three-dimensional objects by layering raw materials in a structured pattern [3]. This innovative method allows the creation of intricate components without the requirement for molds, resulting in a substantial enhancement of both manufacturing flexibility and efficiency [4]. The American Society for Testing and Materials (ASTM) defines AM as the "processes of joining materials to make products from 3D model data, generally layer upon layer," distinguishing it from subtractive manufacturing that involves material removal and generates scrap [5], [6]. The preference for AM over subtractive manufacturing in today's industry is fueled by its high efficiency, reduced material waste, and accelerated production times, making it particularly suitable for developing prototypes and working models. Directed Energy Deposition (DED), a prominent AM method is gaining prominence in industries that utilize metal as a raw material and involves depositing metal powder or wire feedstock onto a specified area and melting it using energetic sources like lasers, electron beams or arcs, resulting in the formation of a sintered layer on the substrate [7]. Within the spectrum of DED methods, the arc-based Wire Arc Additive Manufacturing (WAAM) technique emerges as a notable approach. In this DED technology, the primary feedstock for shaping the desired product is metal wire, boasting an impressive deposition rate ranging from 50 to 130 grams per minute. The welding torch meticulously delivers the metal wire feedstock to the welding arc at a predetermined rate, where it serves as a fusion source, melting the metal wire feedstock. Subsequently, the molten metal is applied layer by layer onto the substrate, gradually solidifying and giving rise to the intended geometric structure [7]. WAAM has gained widespread popularity owing to its actual attributes, including an increased deposition rate, efficient material utilization, relatively lower production and equipment costs, and high equipment flexibility and scalability across various Additive Manufacturing (AM) processes [8]. Despite its advantages of a faster deposition rate and cost-effectiveness, it's worth noting that WAAM exhibits less precision in terms of dimensions compared to Electron Beam (EB) and laser energy sources. Based on arc welding technology, WAAM is classified into Gas Metal Arc Welding (GMAW)-based [9], Gas Tungsten Arc Welding (GTAW)-based [10] and Plasma Arc Welding (PAW)-based [11]. The Gas Metal Arc Welding (GMAW) technique makes use of a continuously fed, consumable wire electrode and a power source to produce an electrical arc between the electrode and the workpiece. GMAW-based WAAM is extensively favored for its ability to construct thin multi-layer structures, with almost two times higher deposition rates than the GTAW and PAW-based WAAM techniques [12]. While GMAW is acclaimed for its remarkable deposition rate and cost-effectiveness in WAAM, it does come with noteworthy drawbacks. The heightened levels of heat input and weld spatter lead to compromised weld quality, consequently impacting the overall quality of WAAM-manufactured components. In response to these challenges, Cold Metal Transfer (CMT) has emerged as a viable solution, representing a progressive development of the GMAW short arc process. The primary focus in CMT is to minimize the arc burning time, thereby reducing heat input to a minimum. This is achieved by carefully controlling the heat generated, ensuring it is just enough to melt the wire and fuse the base metal. Adding to the sophistication of the welding process, a secondary wire feeder integrated into the torch is employed to introduce a high-frequency reciprocating motion to the wire electrode. This mechanical movement plays a pivotal role in facilitating exceptionally smooth and nearly spatter-free droplet detachment, complemented by a concise arc-burning time. The synergistic effect of minimized heat input and controlled wire movement significantly enhances the overall efficiency and quality of the CMT welding process [13]. Austenitic stainless steels (ASS), known for their remarkable resistance to corrosion, outstanding formability, and consistent mechanical strengths at various temperatures, are extensively employed across

multiple sectors, demonstrating enduring durability. Owing to its robustness, ability to withstand elevated temperatures and anti-corrosion properties, especially in demanding environments, this material finds prevalent use in applications such as nuclear reactors [14], boilers [15], pipelines [16], heat exchangers [17], industries related to oil, gas, and chemicals [18]. Food processing sector [19], production of medical devices and implants [20], and making offshore oil and gas pipelines [21]. WAAM prefers the 300 series of ASS, particularly SS316L, for its adaptability in manufacturing complex metal parts with stringent performance criteria. This material is extensively utilized across several industries, including aerospace, automotive, oil and gas, marine, and general manufacturing [22]. Hence, there's a significant emphasis on research concerning SS316L, given its extensive utility in sectors considered to be at the forefront of technological advancement

Research on CMT-based WAAM of SS316L parts is relatively limited. There is a lack of comprehensive investigations addressing spatial variations in microstructural features across built parts and their correlation to the WAAM procedure. This study aims to bridge this gap by thoroughly examining the SS316L CMT-based WAAM wall. A wide range of material characterization techniques were employed to achieve a thorough evaluation of the as-deposited CMT wall. These encompass analyses of macroscopic morphology, evolution of microstructure, mechanical behavior, Field Emission Scanning Electron Microscopy (FESEM) examination, X-ray Diffraction (XRD) for phase identification, Energy-Dispersive Spectroscopy (EDS) for assessing elemental distribution, assessment of wear resistance, analysis of surface topography, and evaluation of resistance to corrosion.

2. Experimental Configuration

In this study, the AM setup utilized a CMT welding unit (Fronius TPS 400i) as the primary heat source for the deposition process. The management system consisted of a wire feeder (Fronius WF 25i REEL-R) and a robot (Kawasaki). **Figure 1** illustrates the experimental arrangement, highlighting the essential components employed in this research.

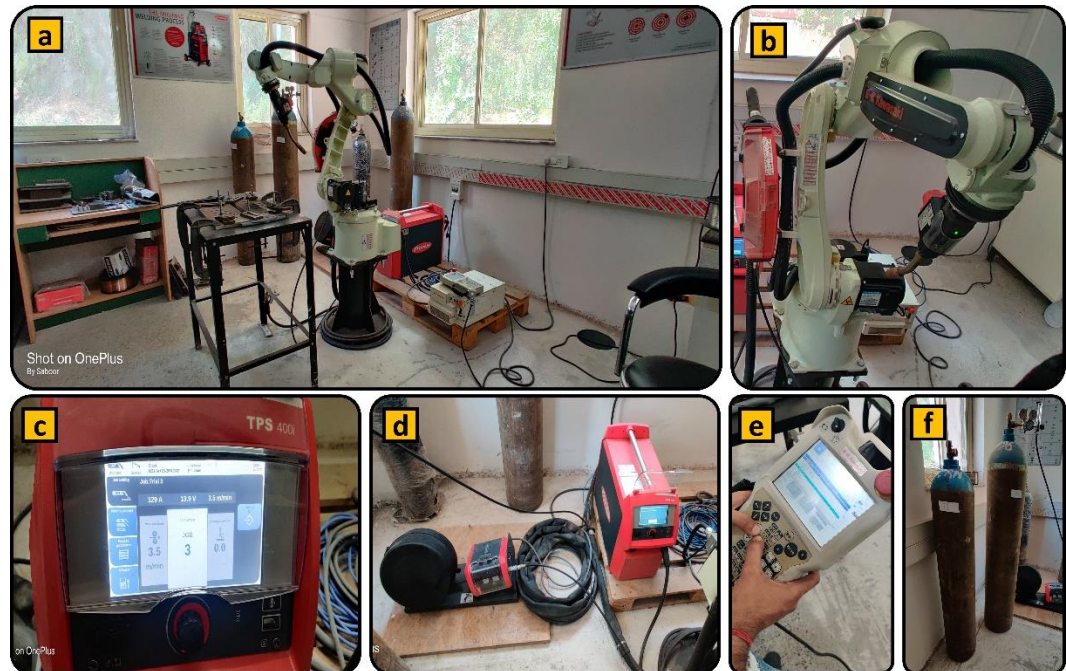


Figure 1.

- Experimental WAAM system:
 (a) CMT based WAAM setup;
 (b) Robotic arm;
 (c) Welding power source;
 (d) Wire feeder;
 (e) Robot control pendant;
 (f) Argon gas cylinders

3. Material and Fabrication

The wire feedstock chosen for this experiment was a 1.2 mm diameter SS316L wire utilized for deposit production. The elemental composition of the SS316L wire is presented in **Table 1**.

Table 1.
 Chemical composition (wt%) of SS316L wire used in this study (Producer's data sheet)

C	Mn	Si	S	P	Cr	Ni	Mo	N	Cu	Nb
0.021	1.63	0.36	0.009	0.039	16.84	10.08	2.06	0.052	0.22	0.025

Table 2.
Deposition process parameters used for fabrication of SS316L CMT-based WAAM wall

Process Parameters	Values
Voltage	13.9 V
Current	130 A
Wire feed rate	3500 mm/min
Travel speed/Scanning speed	350 mm/min
Contact tip distance	3 mm
Wire out distance	14 mm
Shielding gas	Argon
Shielding gas flow rate (Argon)	16 L/min

For the deposition process, an SS304 served as the substrate. The deposition path of molten metal was bi-directional which was controlled by robot (Kawasaki). This path helped in creation of uniform and consistent beads. The deposition parameters are listed in [Table 2](#). To ease heat buildup and help cooling between deposited layers, a dwell time of

90 seconds was implemented after each layer. Following the fabrication of CMT based WAAM wall as depicted in [Figure 2](#), the SS304 substrate was cut and separated from the manufactured portion with the removal of the stair step effect using the wire EDM (Electrical Discharge Machining). Post-machining, samples were extracted from various locations (upper, middle, lower) of the as-built wall to facilitate a comprehensive range of experiments.

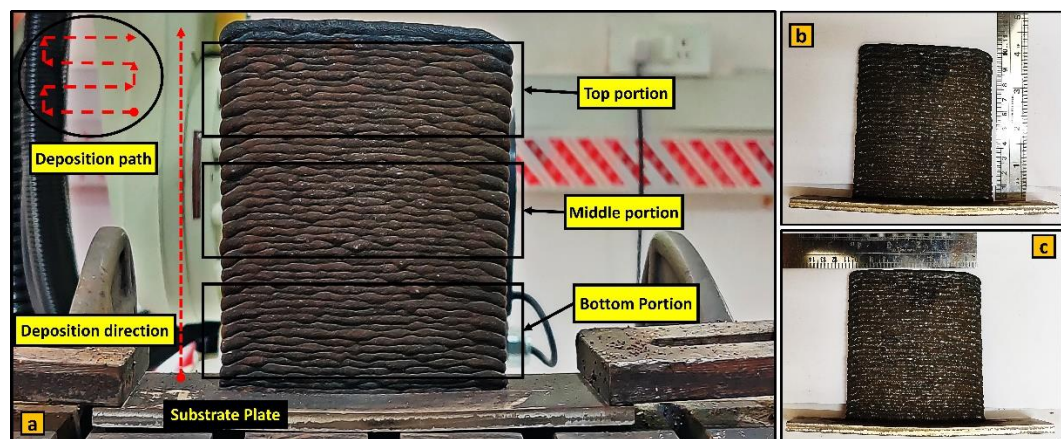


Figure 2.
CMT based WAAM fabricated wall

4. Testing and Characterization

4.1. Macroscopic and Microstructural Characterization

To analyze the microstructural properties in the deposited walls, samples were extracted from the lower, middle, and upper portions across the deposition direction using the wire EDM process. After the extraction, the samples underwent standard grinding procedures. Subsequent to the grinding process, the samples were polished with abrasive paper, ranging in grit sizes from 100 to 2500, to facilitate metallographic analysis. Following polishing, the samples underwent electrochemical etching, with the voltage set to 10V and the etching time fixed at 15 seconds, using a 10% oxalic acid solution as an etchant. The specimens extracted underwent examination using an optical microscope (Leica DM6000M) and an electron microscope (Zeiss GeminiSEM 500) for comprehensive microstructural analysis. Energy dispersive spectroscopy (EDS) analyses were also conducted (Octane elect plus EDAX). Moreover, the phase characterization was conducted using the X-ray diffraction (XRD) method (Rigaku Smart Lab).

4.2. Mechanical Property Characterization

Vickers microhardness testing was conducted across the deposition direction using a microhardness tester (Tinius Olsen FH-4 series), applying a consistent indentation load of 1kgf with a dwell time of 15 seconds per indentation point. Charpy V-notch impact testing involved a total of nine samples extracted horizontally from the lower to the upper section of the as-built wall using a wire EDM machine. The Charpy test specimen deviated from the international standard ASTM E23 by being smaller than the prescribed minimum dimensions. To meet standard requirements, the specimen dimensions were proportionally scaled down and were standardized to dimensions of 55 × 10 × 5 mm. Following this adjustment, the samples underwent machining to achieve a smooth finish. Testing occurred using an impact testing machine (Walter+bai PH-300) at room temperature, with the notch of the Charpy V-notch sample-oriented perpendicular to the depositing direction of the built-up wall. Tensile testing was carried out on two samples obtained from the upper, middle, and lower sections of the as-built wall. using a wire EDM machine. The

tensile specimens were smaller than the minimum dimensions stipulated by the international standard. To conform to standard requirements, the specimen dimensions were proportionally reduced [23]. The tests were executed universal testing machine (Tinius Olsen 100ST) at room temperature (24 ± 2 °C), employing a uniform strain rate of 2 mm/min. Fracture surface morphologies of the tensile and Charpy specimens were analyzed using an electron microscope (Zeiss GeminiSEM 500) and EDS (Octane elect plus EDAX).

4.3. Tribological Performance

Tribological performance across the deposition direction at the upper, middle, and lower sections of the CMT-based WAAM wall was studied through the dry reciprocating sliding wear test. Testing was conducted on the engine tribometer with tribo-corrosion (RTec instrument – MFT-5000). The stroke length, reciprocating frequency, and scanning time were held constant at 2 mm, 15 Hz, and 10 min, respectively, under three distinct loading conditions: 15 N, 20 N, and 25 N. Electron microscope (Zeiss GeminiSEM 500) and EDS (EDAX Octane Elect Plus) was used to analyze the wear tracks and its elemental composition, which allowed to study the mechanism of wear.

5. Results and Discussion

5.1. Macrostructure Morphology

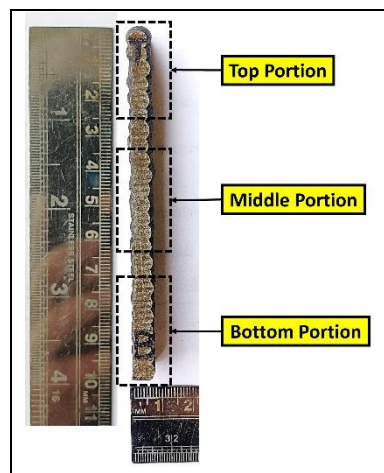


Figure 3.
Cross sectional view
of CMT based WAAM
fabricated wall

The macroscopic examination of the as-deposited wall's cross-sectional view, as presented in Figure 3, shows a neat and orderly weld bead without any evidence of metal distortion or collapse on the wall's surface. The macrostructure of the wall is characterized by distinct layers with arc-shaped fusion lines. The deposited layers were without visible interfaces thus indicating a perfect fusion of the layers. The lack of any porosity, distortion, or warping within the structure points to the absence of defects in the fabricated wall. These observations endorse the effective application of the CMT process in creating SS316L walls through WAAM. Additionally, it was noted that the base of the as-deposited wall showed a narrower width due to the rapid cooling by the substrate on the initial layers. As the deposition process continued, the heat buildup from the

consistent arc heating slowed the rate of solidification in the molten pool, allowing the liquid metal more time to flow laterally. Consequently, there's a noticeable widening of the cross-section's width upwards across the deposition direction.

5.2. Microstructural Morphology

Microstructural analysis was conducted on a transverse cross-section of an SS316L CMT-based WAAM wall. The study focused on the lower, middle, and upper sections, as illustrated in Figure 4. The as-deposited wall displayed a distinctive layer-belt microstructural pattern. This pattern was the result of a procedure in which each layer of molten metal was layered and solidified on top of the one before it. During the layering process, the heat from both the transitioning droplets and the welding arc caused a partial re-melting of the current layer. This re-melting process was crucial for creating a melt pool on the surface of the layer that had just been laid down. The already-placed layer aided in nucleation, causing heterogeneous nucleation to occur on its surface. At the same time, the energy of the arc propelled the transitioning droplet into the molten pool at an exceptionally high velocity. This collision produced a circular moving flow field within the melt pool, significantly disrupting the forming dendrites. The agitation caused by the flow fragmented the dendrites, making them smaller and enabling the formation of a greater number of finer dendrites. As the arc shifted away from the area, the strength of the stirring flow field saw a gradual decrease. This decline permitted the tiny dendrites to extend vertically upwards along the thermal gradient. The dendrites expanded until they surfaced at the melt pool's top. This cycle of layering, re-melting, and dendritic expansion persisted with each pass of the arc until the deposition was fully accomplished. The end result was a precise layered microstructure, achieved by the careful manipulation of the deposition settings and thermal

dynamics. Also, across the deposition direction, it was observed that the lower section had fine equiaxed dendritic grains. The reason is that the lower sections experienced significantly high cooling rates during the solidification process due to the temperature of the substrate plate being at ambient temperature. In the middle region, columnar grains with vertically oriented and well-aligned dendrites were seen. The top region displayed an elongated coarse columnar dendritic structure. The transition from fine equiaxed grains to coarser columnar grains from the lower to the upper section across the deposition direction was influenced by the decreasing temperature gradient and increasing heat accumulation. The addition of deposited layers from the bottom to the top led to a reduction in cooling rates due to the diminishing temperature gradient. FESEM observation as depicted in Figure 4b, Figure 4d, Figure 4f revealed that the δ -ferrite (BCC) was embedded in the austenite matrix (FCC) and their distribution was randomly. Regarding ferrite morphology, it was observed that the lower section is characterized by globular and skeletal ferrites, the middle portion by vermicular and skeletal ferrites, while the top portion consists of acicular and lathy ferrite combination lathy structures.

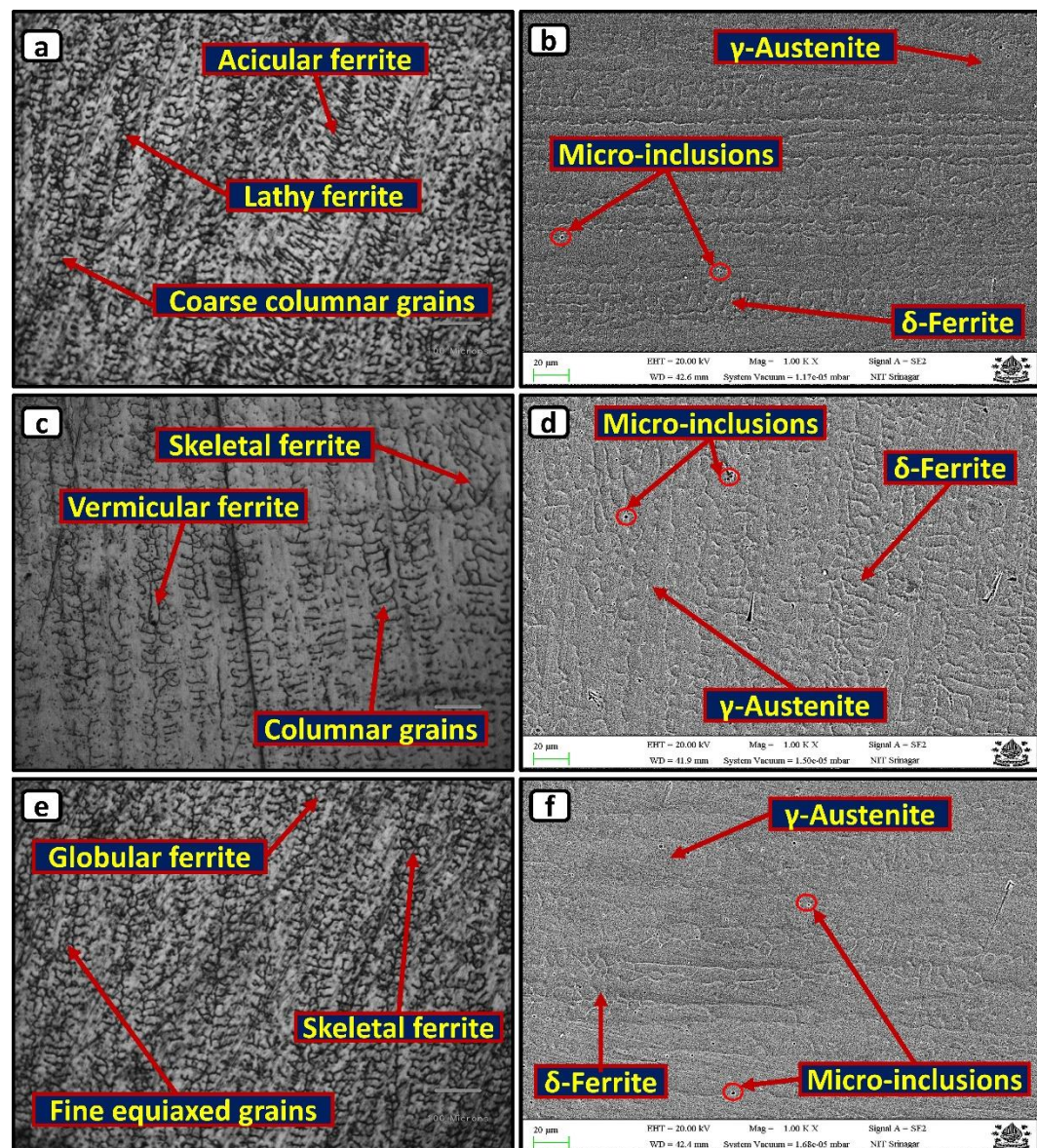


Figure 4. Optical and FESEM images of CMT based WAAM wall across deposition direction: (a,b) optical and FESEM image of top portion; (c,d) optical and FESEM image of middle portion; (e,f) optical and FESEM image of bottom portion

5.3. X-ray Diffraction Analysis

The XRD spectrum obtained for the top, middle and bottom portion of the fabricated wall are depicted in Figure 5. The peaks strongly show the presence of ferrite phase at (111) within the bottom regions while the top layers show greater existence of austenite phase at (022). Observation clearly indicates that as we move across the deposition direction from bottom region to the top region, the peaks of ferrite decreases while the peaks of austenite increases. This result

validates that as we move from bottom to top portion of the fabricated wall, the dissolution and decreases of concentration of ferrite takes place while the austenite concentration increases.

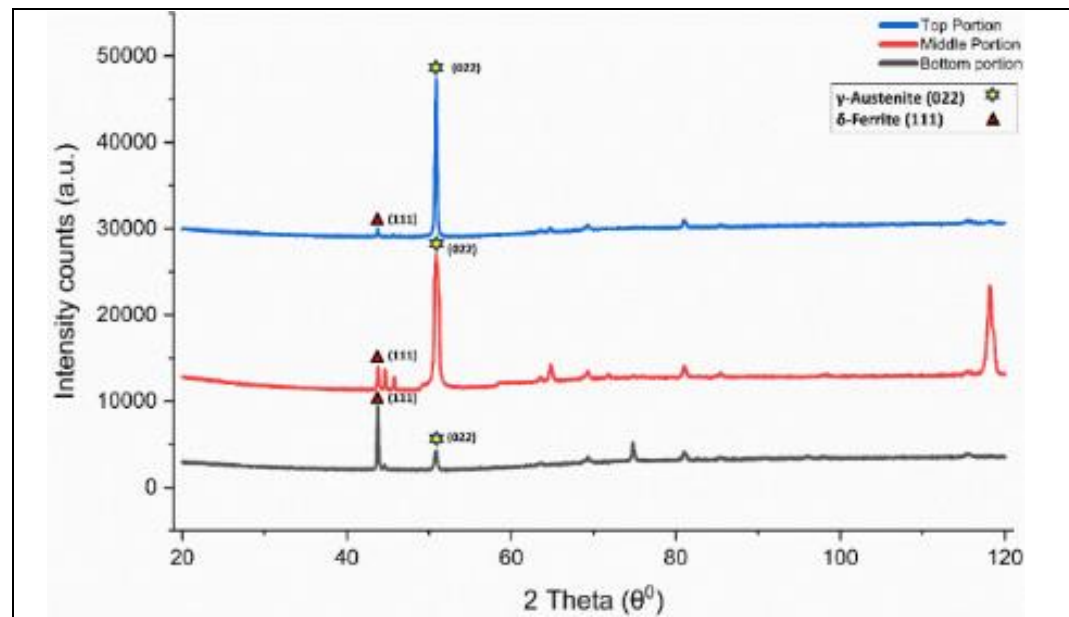


Figure 5. Phase identification of CMT based WAAM wall across deposition direction (top, middle and bottom portion)

5.4. Mechanical Property Characterization

The mechanical performance of the CMT-based WAAM wall at room temperature was evaluated using Vickers microhardness tests, the Charpy impact test, and the Uniaxial tensile test.

5.4.1. Vickers Microhardness Testing

The hardness curve, as depicted in **Figure 6**, is divided into bottom, middle, and top portions. Observation indicates a descending trend in hardness values from the lower to the upper regions. Specifically for the upper, middle, and lower portions, the average microhardness value stands at 177.83 HV, 182.19 HV, and 183.16 HV, respectively. Across the entirety of the fabricated wall, across the deposition direction, the average microhardness value stood at 181.05 HV, with a maximum and minimum value being 189.4 HV and 170.9 Hv, respectively. The standard deviation and range stood at 3.75 and 18.5, respectively. The variation in microhardness is linked to the heterogeneous microstructure across the deposition direction of components manufactured using WAAM. The heightened microhardness observed in the lower portion can be ascribed to enhanced heat dissipation through the substrate, leading to a more rapid cooling process, the formation of a fine dendritic microstructure, and an elevated concentration of ferrite. Furthermore, the accumulation of multiple transient thermal cycles with varying heat amplitudes was sustained in the lower region due to the continuous deposition of several layers from the bottom to the top.

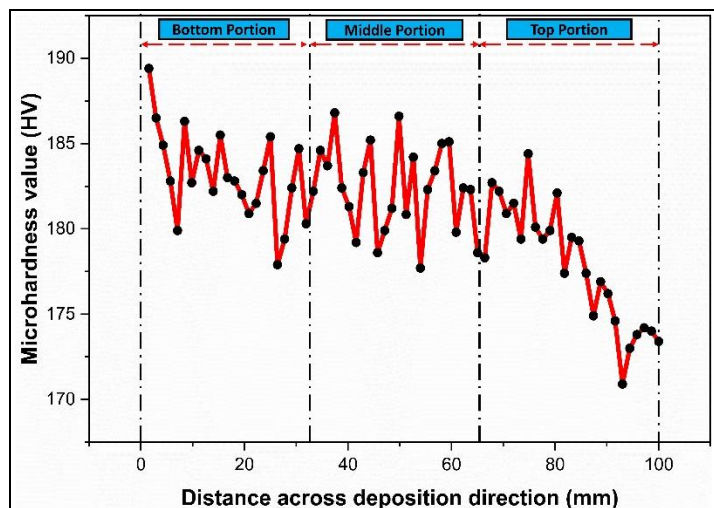


Figure 6. Vickers hardness distribution profile of CMT based WAAM wall across deposition direction

Conversely, the upper portion, characterized by coarser structures, exhibited a slower cooling rate and increased heat retention, resulting in lower microhardness values. Notably, the hardness in the lower section was marginally higher than that in the upper part. The microhardness values in the intermediate layers remained relatively constant, indicating a state of equilibrium between heat input and dissipation.

5.4.2. Charpy V-Notch Impact Testing

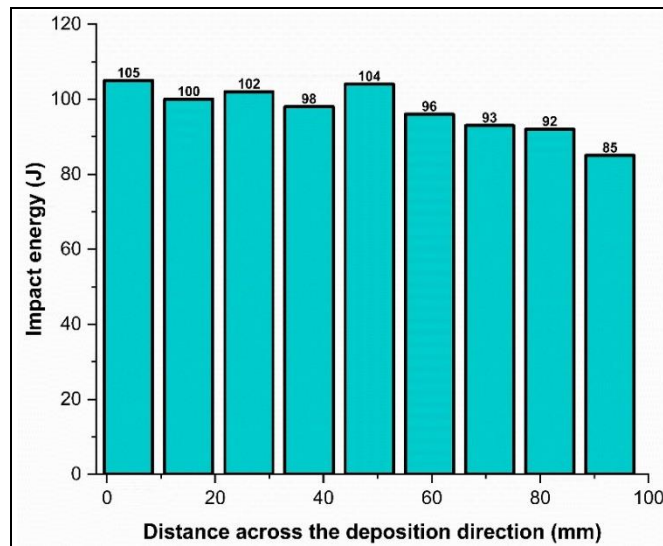


Figure 7.
Impact energy
variation of fractured
Charpy V-notch
samples taken across
deposition direction

Charpy V-notch impact testing was carried out on the lower, middle, and upper portions of the CMT-based WAAM wall, with three horizontal samples obtained from each position across the deposition direction. As depicted in [Figure 7](#), a clear decreasing trend in impact energy is observed in the horizontal Charpy V-notch samples from the lower to the upper portion of the wall. The lower sections of the wall exhibit slightly higher average energy values compared to the middle and top sections, with values being 102.23 J, 99.33 J, and

90 J, respectively. This disparity in energy values at the lower portion is attributed to the faster cooling rate and fine dendritic microstructure. The average impact energy value for all samples across the deposition direction stood at 97.22 J. The maximum impact energy value was related to the lower portion sample with a value being 105 J, and the minimum value was related to the upper portion sample with a value being 85 J. The standard deviation and range stood at 6.45 and 20, respectively, for the entirety of the wall.

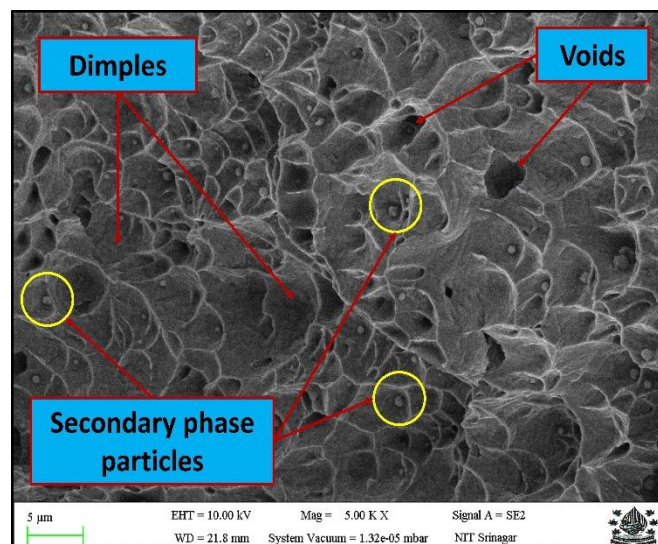


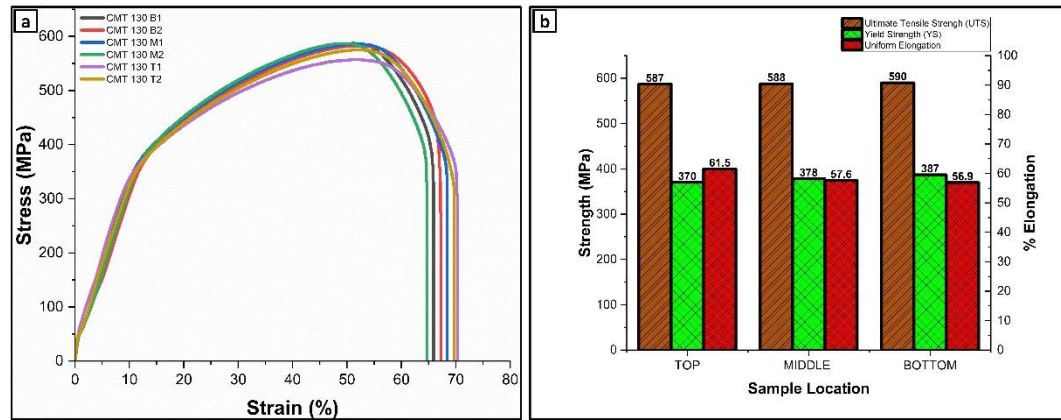
Figure 8.
FESEM analysis of
fractured Charpy V-
notch sample

Fractographic analysis using a FESEM image of the Charpy V notch sample taken from the middle portion of the wall is depicted in [Figure 8](#). The results indicate a prominent presence of significant dimples, signifying the ductile behavior of the samples. The impressive ductility observed in the multilayer deposited sample is supported by its strength, as determined from the Charpy impact test results. Furthermore, the absence of small cracks or holes on the damaged object's surface further confirms its robust impact characteristics.

5.4.3. Uniaxial Tensile Testing

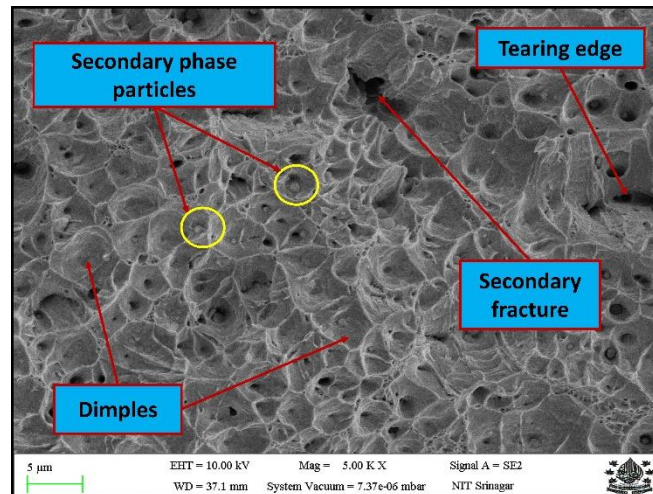
The mechanical behavior of materials, especially their maximum tensile strength and yield strength, stands as the primary focus of research since these attributes offer insights into the material's reliability and longevity. Specifically, concerning AM, these metrics serve as indicators of the printing process's quality. The stress-strain plot of all samples is depicted in [Figure 9a](#). All tensile samples exhibit failure within the gauge length. The 0.2% yield strength was calculated from the stress-strain plot for all the samples. The plot distinctly demonstrates plastic deformation occurring before reaching the fracture point. This serves as a clear indication that the SS316L wall fabricated through CMT-based WAAM exhibits significant ductility. [Figure 9b](#) provides the average yield strength (YS, 0.2% offset), average ultimate tensile strength (UTS), and average %elongation values of two samples, each from the upper, middle, and lower portion of the CMT-based WAAM wall. The average YS and UTS for tensile samples from the upper section are 370 ± 4.96 MPa and 587 ± 3.12 MPa. For the middle section are 378 ± 3.16 MPa and 588 ± 2.22 MPa, and for the lower section are 387 ± 1.98 MPa and 590 ± 3.18 MPa. Additionally, The average elongation values for the upper, middle, and lower sections are 61.5, 57.6, and 56.9, respectively.

Figure 9. Uniaxial tensile test results of CMT based WAAM wall across deposition direction: (a) Stress-strain plot of samples from top, middle and bottom portion of wall; (b) Average UTS, YS and %elongation of samples across deposition direction



The results indicate a decreasing trend in YS and UTS values from the lower to the upper section. The observed anisotropy in tensile properties across the deposition direction is attributed to variations in microstructure, including grain morphology and ferrite morphologies. Since all the assessed tensile properties meet the industry standards for SS 316 L, the CMT-based WAAM component complies with the specifications for commercial use.

Figure 10. Fractured uniaxial tensile sample's FESEM analysis



The FESEM image of fractured tensile specimens is depicted in Figure 10. The fractured surface exhibits homogeneously distributed equiaxed-shaped dimples, indicating a ductile fracture mode with good toughness in SS316L CMT-based WAAM-built structures. The morphology of these dimples correlates with the grain size within the built microstructure. Specifically, specimens from the lower portion display deeper and finer dimples compared to the middle and

upper portion. Samples from the top portion show shallower and larger-sized dimples. Furthermore, secondary-phase spherical particles were identified through fractographic research. EDS analysis with elemental mapping of this secondary phase particle is depicted in Figure 11. These particles were identified to be carbides which usually have a capacity to enhance UTS.

5.5. Tribological Performance

5.5.1. Coefficient of Friction

The Coefficient of Friction (COF) is the ratio of the frictional force between two bodies to the applied load [24]. A lower COF typically suggests better lubricity and less friction, which can lead to reduced wear between interacting surfaces. Figure 12 illustrates the COF versus time at different loads for samples across the deposition direction (lower, middle, upper). The results indicate a clear trend with COF increasing with increasing applied load. Specifically, the COF ranges from 0.190 to 0.203 at 15 N, 0.205 to 0.219 at 20 N, and 0.208 to 0.232 at 25 N. This phenomenon can be attributed to augmented contact stress, more pronounced deformation, and modifications in lubrication efficiency. With increased load applied, the contact pressure between the surfaces in contact intensifies. The microstructure evolution from finer equiaxed grain structure to relatively coarser columnar grain structure happens across the deposition direction. The lower portion has a finer grain structure than the top portion. In general, materials with a finer grain structure tend to have lower coefficients of friction (COF) compared to those with coarser grain structures. This is because finer grains often result in a smoother surface texture, reducing the contact area and thereby lowering frictional forces between sliding surfaces. Additionally, fine-grained materials exhibit better lubricant retention and distribution, further contributing to lower COF during wear tests.

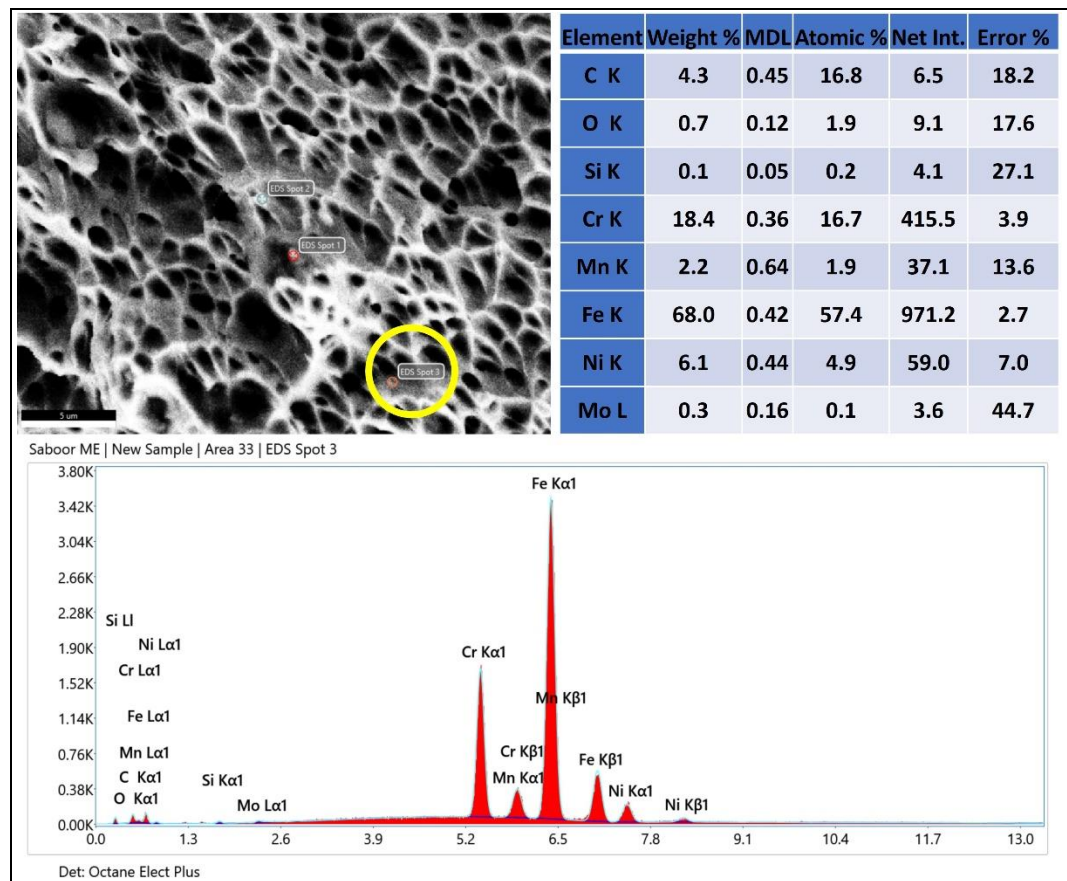


Figure 11.
EDS result of spherical
particle present in
dimples of fractured
tensile sample

5.5.2. Wear Rate and Specific Wear Rate

The wear rate typically expressed in volume loss (mm^3) per unit of sliding distance (m) and measures loss of material from a surface due to wear with respect to specified time. According to ASTM specification G133-05, the wear rates were determined using the Eq. (1).

$$W_r = \frac{\Delta W / \rho \cdot 1000}{V_s \cdot t} \quad (1)$$

where, for the sliding wear test, ΔW (g) represents mass loss, ρ (g/cm^3) represents density, V_s (m/s) represents sliding velocity, and t (s) stands for time duration. The data in **Figure 13a** reveal that with an upsurge in loading conditions from 15 N to 25 N, the wear rate increases across samples taken from the lower, middle, and upper portions. The wear rate range for the upper portion is slightly higher, with values being $1.74 \times 10^{-3} \text{ mm}^3/\text{m}$ at 15 N load to $2.10 \times 10^{-3} \text{ mm}^3/\text{m}$ at 25 N load, while the lower portion has a wear rate of $1.59 \times 10^{-3} \text{ mm}^3/\text{m}$ at 15 N and $2.08 \times 10^{-3} \text{ mm}^3/\text{m}$ at 25 N. An increase in wear loss can be interpreted through the perspective that an increased load leads to higher stress on the layers below the surface, which in turn causes subsurface initiation of cracks under the load applied [25]. Once reaching a certain critical size, these cracks become unstable and propagate towards the surface. This results in the creation of flake-like debris and substantial pits due to the intense deformation of the surface that has been worn. It was also noted that increased load slightly broadens the track width but more significantly increases the number of contact points linearly, thus elevating the total wear loss. As the surface undergoes greater stresses and deformation, this leads to an escalation in material loss as well as in the forces of friction. Also, the lower portion has a fine-grained structure. Finer grains have high hardness, a relationship given by the Hall-Petch equation. According to Archard's equation, there is an inverse relationship between wear loss and the hardness of the material [26].

Figure 12. Variation of COF vs time at applied loads of 15 N, 20 N and 25 N: (a,b,c) bottom, middle and top portion variation of COF vs time at 15 N; (c,e,f) bottom, middle and top portion variation of COF vs time at 20 N; (g,h,i)) bottom, middle and top portion variation of COF vs time at 25 N

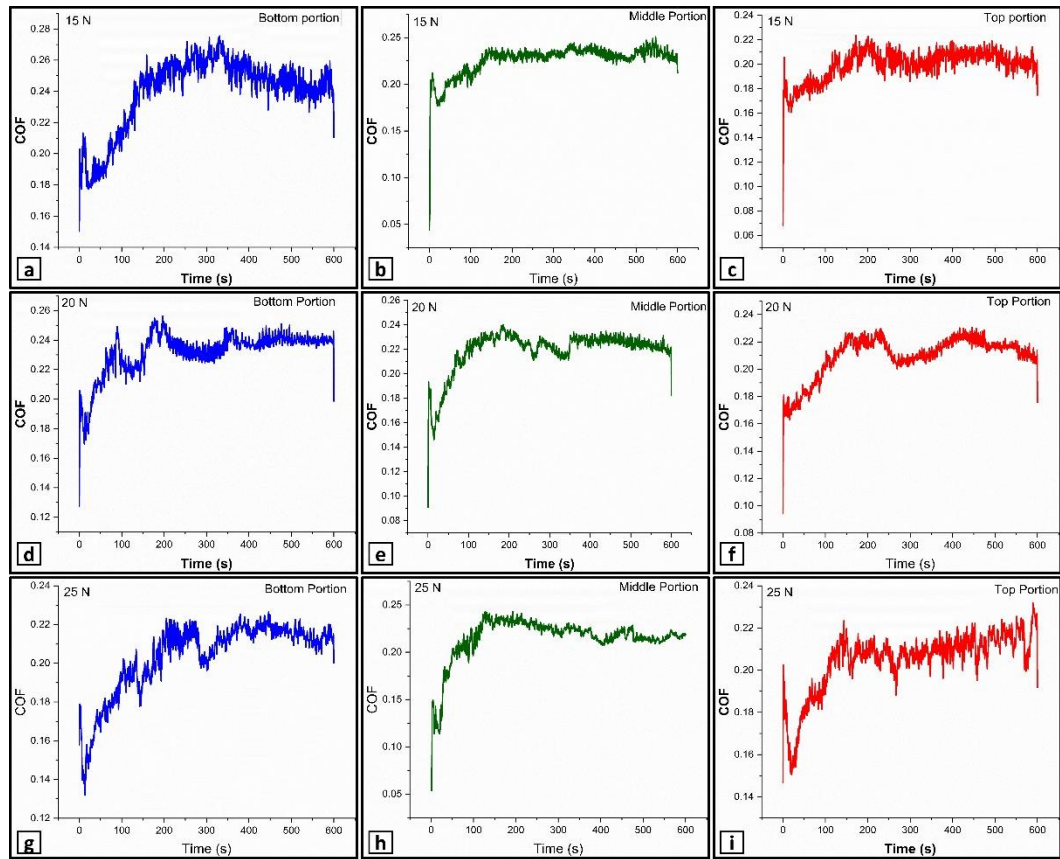
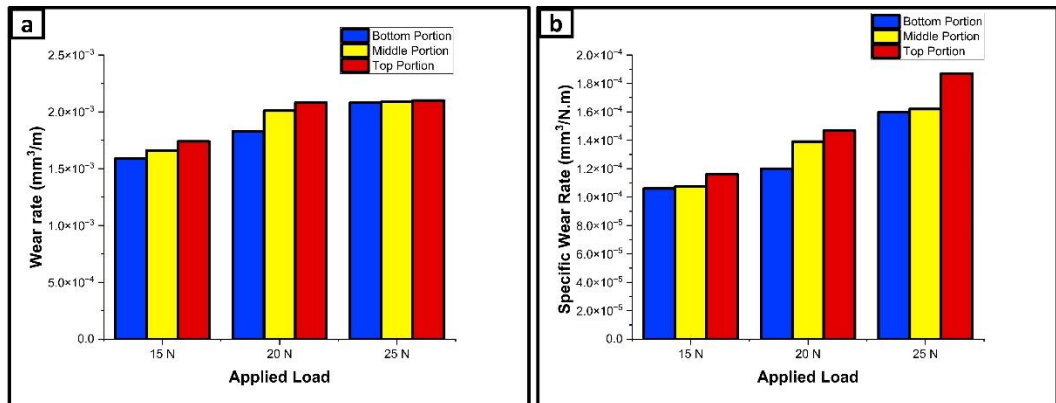


Figure 13. (a) Wear rate variation with applied load of 15 N, 20 N, and 25 N for top, middle and bottom portion samples (b) Specific wear rate variation with applied load of 15 N, 20 N, and 25 N for top, middle and bottom portion samples



$$V = \frac{K.F.L}{H} \tag{2}$$

V (mm³) is the volumetric wear loss, K represents the dimensionless wear coefficient, which depends on the materials in contact, F (N) denotes the applied normal load, L (mm) denotes the sliding distance, and H (HV) is the hardness of the softer material in the contact pair. The wear rate (mm³/m) is directly proportional to the wear loss (mm³) [27]. This validates the lower wear rate of the lower portion compared to upper portion. The specific wear rate (*S_{wr}*), also known as the wear coefficient, represents the volume of material lost due to wear per unit of applied load (N) and sliding distance (m). Specific wear rate calculation was performed using the Eq. (3).

$$S_{wr} = \frac{\Delta V}{P.S} \tag{3}$$

ΔV (mm³) represents the volumetric wear loss, P (N) is the force applied, and S (mm) is the sliding distance. The specific wear rate mirrors the same trend as the wear rate, as depicted in Figure 13b. The data reveal that with an increase in loading conditions from 15 N to 25 N, the specific wear rate increases. Specifically, for the lower portion at loads of 15 N, 20 N, and 25 N, the specific wear are 1.061×10^{-4} mm³/N-m, 1.388×10^{-4} mm³/N-m, and 1.597×10^{-4} mm³/N-m, respectively. For the

middle portion, these values were $1.215 \times 10^{-4} \text{ mm}^3/\text{N-m}$, $1.389 \times 10^{-4} \text{ mm}^3/\text{N-m}$, and $1.620 \times 10^{-4} \text{ mm}^3/\text{N-m}$, respectively. Similarly, for the top portion, the values were $1.319 \times 10^{-4} \text{ mm}^3/\text{N-m}$, $1.467 \times 10^{-4} \text{ mm}^3/\text{N-m}$, and $1.984 \times 10^{-4} \text{ mm}^3/\text{N-m}$, respectively.

5.5.3. Wear Track Morphology

FESEM analysis of the wear track, as depicted in Figure 14 reveals parallel grooves, scratches, craters, patches, and delamination, accompanied by cracks, indicating abrasive action. The wear debris is typically small, angular particles, characteristic of abrasive wear. Patches were also present, where material from the CMT-based WAAM wear samples surface adhered to the WC, which validated the occurrence of adhesion wear, but its effect was not dominant. Oxidized regions on the wear track appeared as high-contrast textured patches. All the FESEM observations suggest the wear mechanism to be predominantly abrasive in nature with elements of adhesion, oxidation, and deformation [28].

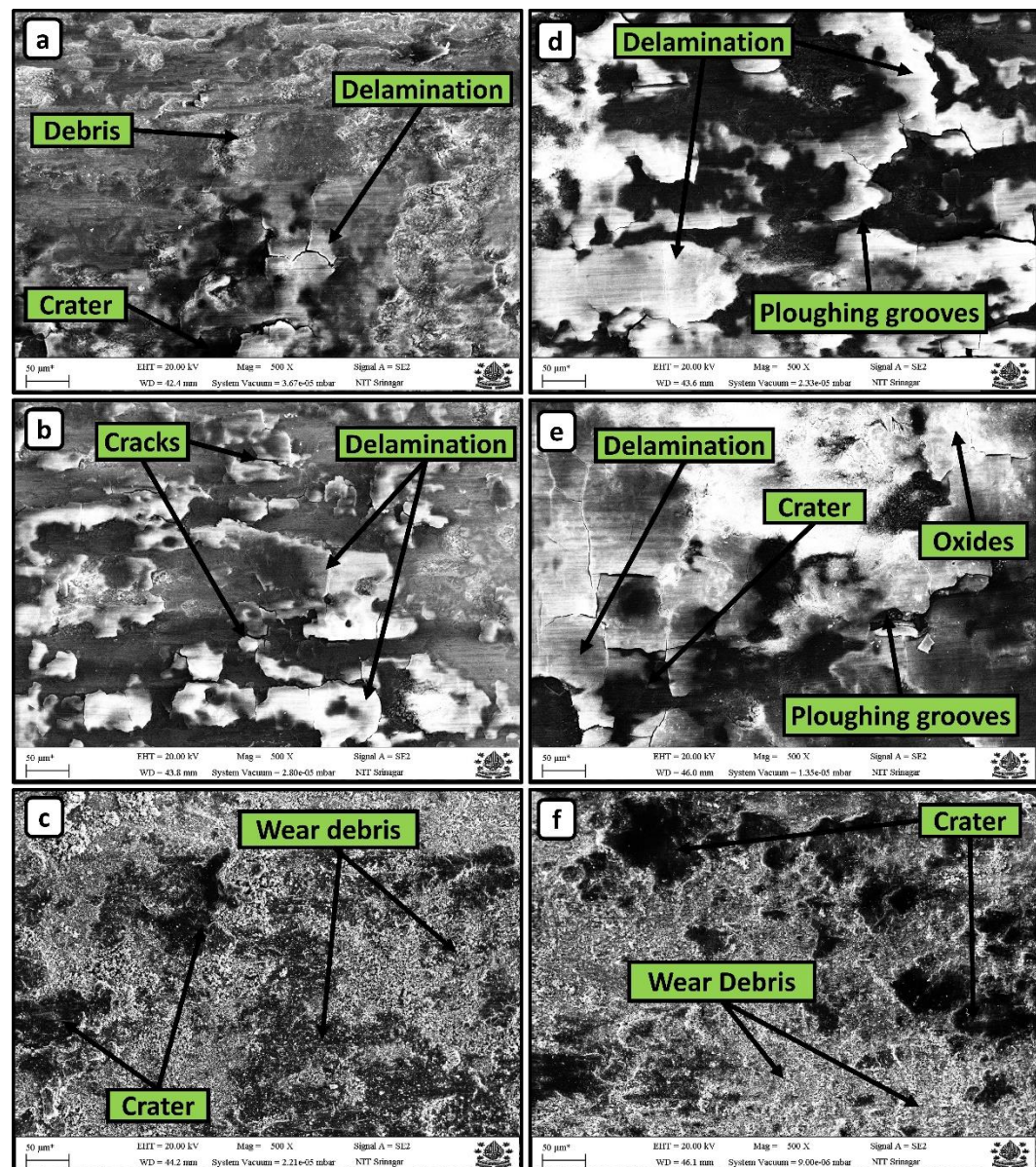


Figure 14. FESEM analysis of wear tracks: (a,b,c) top, middle and bottom portion wear tracks at applied load of 15 N; (d,e,f) top, middle and bottom portion wear tracks at applied load of 25 N

The EDS analysis of the wear scar reveals as depicted in Figure 15 several key insights into its composition and the effects of wear. The wear scar micrograph, taken at a magnification scale of $200 \mu\text{m}$, displays a rough surface typical of mechanical wear, indicating the occurrence of significant material abrasion. Elemental mapping shows the presence and distribution of various elements across the wear scar area. Nitrogen is present in very small quantities (0.1 wt%, 0.2 at%). Oxygen is found in high concentration (15.6 wt%, 36.6 at%), indicating substantial oxidation had occurred, which is common caused due to exposure of wear scar to air. Tungsten is present in

smaller quantities (1.0 wt%, 0.2 at%), which is the indication of the counter body (WC) particles being adhered to SS316L sample and thus validating the occurrence of partial adhesion wear mechanism.

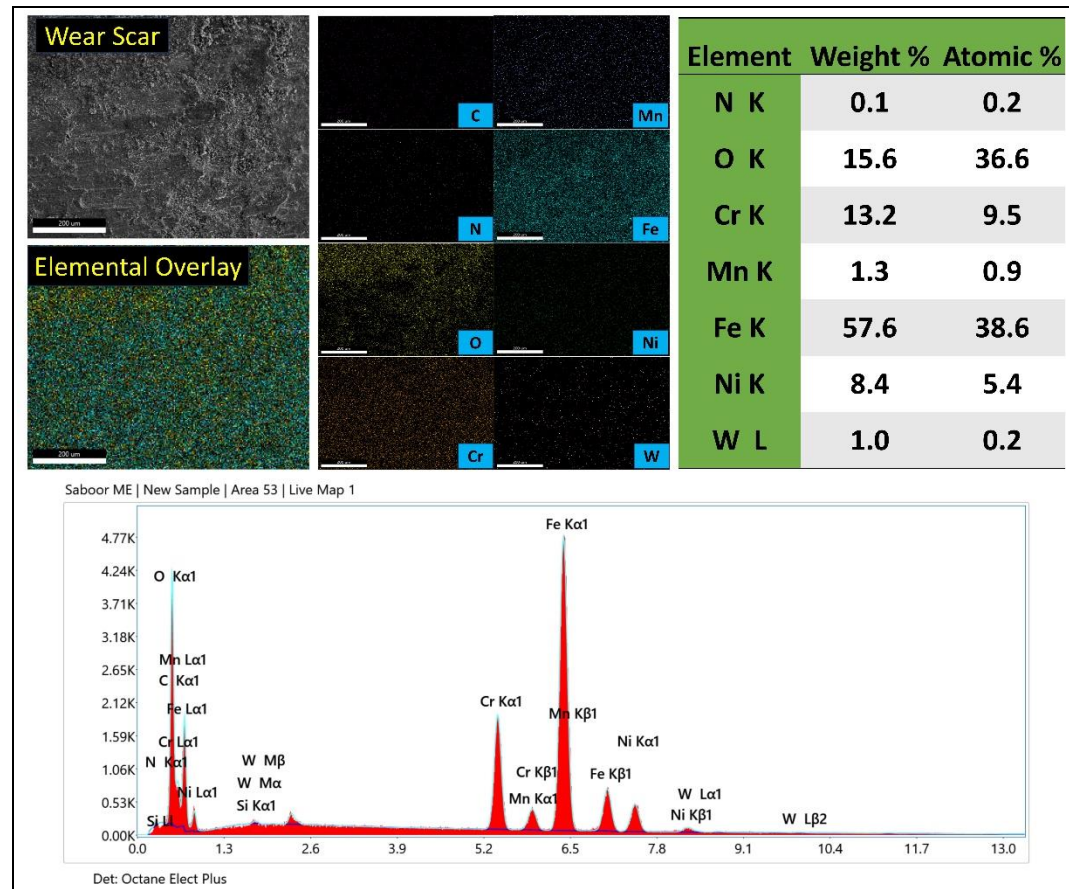


Figure 15.
EDS analysis of wear scar with elemental mapping and elemental distribution

6. Conclusion

In this study, a multilayered wall made of SS316L wire was effectively deposited utilizing the CMT-based WAAM process. The investigation involved a thorough examination of the morphological characteristic, microstructural evolution, mechanical properties, and tribological performance of the SS316L wall across the deposition direction. Based on the investigation, the following conclusions were made:

- A slender and upright SS316L multilayered wall was successfully produced, indicating the feasibility of employing CMT-based WAAM for the fabrication of SS316L alloy structures. The multilayered SS316L fabricated wall exhibited seamless fusion across the deposition direction with the absence of macroscopic defects, such as pores, solidification cracks, and delamination.
- The microstructure analysis reveals fine equiaxed grains with globular and skeletal ferrites in the lower sections. The middle section had fine columnar grains with skeletal and vermicular ferrites while the upper section had coarser columnar grains with acicular and lathy ferrites. FESEM analysis of microstructure revealed the presence of δ -ferrite within the γ -austenitic matrix with the addition of micro-inclusions.
- The Vickers microhardness distribution profile demonstrates a decreasing trend across the deposition direction. Specifically for the upper, middle, and lower portions, the average microhardness value stands at 177.83 HV, 182.19 HV, and 183.16 HV, respectively.
- The analysis of the Charpy impact test showed a noticeable decreasing trend in impact energy across the deposition direction. The lower sections of the wall exhibit slightly higher average energy values compared to the middle and top sections, with values being 102.23 J, 99.33 J, and 90 J, respectively. FESEM analysis of fractured samples reveals the presence of dimples, indicating the ductile behavior of the samples.
- Uniaxial tensile testing of SS316L CMT-based WAAM-built structures shows all samples undergo plastic deformation before fracturing within the gauge length. Yield strength (YS) and ultimate tensile strength (UTS) decrease from the lower to upper sections: upper section YS

and UTS are 370 ± 4.96 MPa and 587 ± 3.12 MPa, middle section are 378 ± 3.16 MPa and 588 ± 2.22 MPa, and lower section are 387 ± 1.98 MPa and 590 ± 3.18 MPa. Elongation averages are 61.5% for the upper section, 57.6 for middle and 56.9 for the lower sections. FESEM analysis of fracture surfaces shows homogeneously distributed equiaxed-shaped dimples, indicating a ductile fracture mode with good toughness.

- f. The coefficient of friction (COF) increased with higher applied loads and from the lower to the upper portion of the deposition. COF ranged from 0.190 to 0.203 at 15 N, 0.205 to 0.219 at 20 N, and 0.208 to 0.232 at 25 N.
- g. The wear rate rose with increasing applied loads from 15 N to 25 N and from the lower to upper portions. The highest wear rate was 2.10×10^{-3} mm³/m for the upper portion at 25 N, while the lowest was 1.59×10^{-3} mm³/m for the lower portion at 15 N. The sliding wear mechanism was pre-dominantly abrasive wear, with partial adhesion wear, oxidative wear, and fatigue wear.

Authors' Declaration

Authors' contributions and responsibilities - The authors made substantial contributions to the conception and design of the study. The authors took responsibility for data analysis, interpretation, and discussion of results. The authors read and approved the final manuscript.

Funding – No funding information from the authors.

Availability of data and materials - All data is available from the authors.

Competing interests - The authors declare no competing interest.

Additional information – No additional information from the authors.

References

- [1] Z. Lin, C. Goulas, W. Ya, and M. J. M. Hermans, "Microstructure and mechanical properties of medium carbon steel deposits obtained via wire and arc additive manufacturing using metal-cored wire," *Metals*, vol. 9, no. 6, 2019, doi: 10.3390/met9060673.
- [2] A. Olszówka-Myalska, M. Godzierz, J. Myalski, and P. Wrześniowski, "Magnesium matrix composite with open-celled glassy carbon foam obtained using the infiltration method," *Metals*, vol. 9, no. 6, 2019, doi: 10.3390/met9060622.
- [3] H. Xin, I. Tarus, L. Cheng, M. Veljkovic, N. Persem, and L. Lorich, "Experiments and numerical simulation of wire and arc additive manufactured steel materials," *Structures*, vol. 34, no. June, pp. 1393–1402, 2021, doi: 10.1016/j.istruc.2021.08.055.
- [4] R. L. Truby and J. A. Lewis, "Printing soft matter in three dimensions," *Nature*, vol. 540, no. 7633, pp. 371–378, 2016, doi: 10.1038/nature21003.
- [5] ASTMStandardF2792, "Standard Terminology for Additive Manufacturing Technologies," *ASTM International*, pp. 1–3, 2015.
- [6] O. Ivanova, C. Williams, and T. Campbell, "Additive manufacturing (AM) and nanotechnology: Promises and challenges," *Rapid Prototyping Journal*, vol. 19, no. 5, pp. 353–364, 2013, doi: 10.1108/RPJ-12-2011-0127.
- [7] C. R. Cunningham, J. M. Flynn, A. Shokrani, V. Dhokia, and S. T. Newman, "Invited review article: Strategies and processes for high quality wire arc additive manufacturing," *Additive Manufacturing*, vol. 22. Elsevier B.V., pp. 672–686, Aug. 2018, doi: 10.1016/j.addma.2018.06.020.
- [8] X. Chen *et al.*, "Cold Metal Transfer (CMT) Based Wire and Arc Additive Manufacture (WAAM) System," *Journal of Surface Investigation*, vol. 12, no. 6, pp. 1278–1284, 2018, doi: 10.1134/S102745101901004X.
- [9] J. Ding *et al.*, "Thermo-mechanical analysis of Wire and Arc Additive Layer Manufacturing process on large multi-layer parts," *Computational Materials Science*, vol. 50, no. 12, pp. 3315–3322, 2011, doi: 10.1016/j.commatsci.2011.06.023.
- [10] P. M. Dickens, M. S. Pridham, R. C. Cobb, I. Gibson, and G. Dixon, "Rapid prototyping using 3-D welding," *Solid Freeform Fabrication Proceedings*, pp. 280–290, 1992.
- [11] S. Ríos, P. A. Colegrove, and S. W. Williams, "Metal transfer modes in plasma Wire + Arc additive manufacture," *Journal of Materials Processing Technology*, vol. 264, pp. 45–54, 2019,

doi: 10.1016/j.jmatprotec.2018.08.043.

- [12] B. Wu *et al.*, "A review of the wire arc additive manufacturing of metals: properties, defects and quality improvement," *Journal of Manufacturing Processes*, vol. 35, pp. 127–139, 2018, doi: 10.1016/j.jmapro.2018.08.001.
- [13] G. Posch, K. Chladil, and H. Chladil, "Material properties of CMT—metal additive manufactured duplex stainless steel blade-like geometries," *Welding in the World*, vol. 61, no. 5, pp. 873–882, 2017, doi: 10.1007/s40194-017-0474-5.
- [14] Q. Li, Y. Shen, and P. Han, "Serrated Flow Behavior of Aisi 316l Austenitic Stainless Steel for Nuclear Reactors," *IOP Conference Series: Materials Science and Engineering*, vol. 250, no. 1, 2017, doi: 10.1088/1757-899X/250/1/012013.
- [15] N. Ghosh, P. Kumar Pal, G. Nandi, and R. Rudrapati, "Parametric Optimization of Gas metal arc welding process by PCA based Taguchi method on Austenitic Stainless Steel AISI 316L," *Materials Today: Proceedings*, vol. 5, no. 1, pp. 1620–1625, 2018, doi: 10.1016/j.matpr.2017.11.255.
- [16] S. Kožuh, M. Gojić, L. Vrsalović, and B. Ivković, "Corrosion failure and microstructure analysis of AISI 316L stainless steels for ship pipeline before and after welding," *Kovove Materialy*, vol. 51, no. 1, pp. 53–61, 2013, doi: 10.4149/km_2013_1_53.
- [17] J. P. Solano, D. S. Martínez, P. G. Vicente, and A. Viedma, "Enhanced thermal-hydraulic performance in tubes of reciprocating scraped surface heat exchangers," *Applied Thermal Engineering*, vol. 220, 2023, doi: 10.1016/j.applthermaleng.2022.119667.
- [18] C. C. Silva, J. P. Farias, and H. B. de Sant'Ana, "Evaluation of AISI 316L stainless steel welded plates in heavy petroleum environment," *Materials and Design*, vol. 30, no. 5, pp. 1581–1587, 2009, doi: 10.1016/j.matdes.2008.07.050.
- [19] A. Zaffora, F. Di Franco, and M. Santamaria, "Corrosion of stainless steel in food and pharmaceutical industry," *Current Opinion in Electrochemistry*, vol. 29, 2021, doi: 10.1016/j.coelec.2021.100760.
- [20] T. Hryniewicz, K. Rokosz, and M. Filippi, "Biomaterial studies on AISI 316L stainless steel after magnetoelectropolishing," *Materials*, vol. 2, no. 1, pp. 129–145, 2009, doi: 10.3390/ma2010129.
- [21] D. Li, Q. Liu, W. Wang, L. Jin, and H. Xiao, "Corrosion behavior of aisi 316l stainless steel used as inner lining of bimetallic pipe in a seawater environment," *Materials*, vol. 14, no. 6, 2021, doi: 10.3390/ma14061539.
- [22] L. P. Raut and R. V. Taiwade, "Wire Arc Additive Manufacturing: A Comprehensive Review and Research Directions," *Journal of Materials Engineering and Performance*, vol. 30, no. 7. Springer, pp. 4768–4791, Jul. 2021, doi: 10.1007/s11665-021-05871-5.
- [23] B. Tomar and S. Shiva, "Microstructural and mechanical properties examination of SS316L-Cu functionally graded material fabricated by wire arc additive manufacturing," *CIRP Journal of Manufacturing Science and Technology*, vol. 50, pp. 26–39, 2024, doi: 10.1016/j.cirpj.2024.02.002.
- [24] Q. J. Wang and Y.-W. Chung, *Encyclopedia of Tribology*. Boston, MA: Springer US, 2013.
- [25] M. A. Islam and Z. Farhat, "Wear of A380M aluminum alloy under reciprocating load," *Journal of Materials Engineering and Performance*, vol. 19, no. 8, pp. 1208–1213, 2010, doi: 10.1007/s11665-010-9595-3.
- [26] V. K. Rai, R. Srivastava, S. K. Nath, and S. Ray, "Wear in cast titanium carbide reinforced ferrous composites under dry sliding," *Wear*, vol. 231, no. 2, pp. 265–271, 1999, doi: 10.1016/S0043-1648(99)00127-1.
- [27] Q. Wang *et al.*, "Microstructure and sliding wear behavior of pure titanium surface modified by double-glow plasma surface alloying with Nb," *Materials and Design*, vol. 52, pp. 265–273, 2013, doi: 10.1016/j.matdes.2013.05.061.
- [28] C. Sasikumar and R. Oyyaravelu, "Mechanical properties and microstructure of SS 316 L created by WAAM based on GMAW," *Materials Today Communications*, vol. 38, 2024, doi: 10.1016/j.mtcomm.2023.107807.